

Pore-scale large eddy simulation of turbulent flow and heat transfer over porous media

Mohammad Jadidi, Alistair Revell, Yasser Mahmoudi *

Department of Mechanical, Aerospace and Civil Engineering (MACE), University of Manchester, M13 9PL, UK



ARTICLE INFO

Keywords:

Porous medium
Flow leakage
Porous-fluid interface
Hairpin coherent structures
Kelvin-Helmholtz instability
Large eddy simulation

ABSTRACT

This paper investigates turbulent fluid flow and heat transfer over a porous medium in a channel using pore-scale large eddy simulation. Special attention is placed on the exchange of heat and flow between the porous and non-porous regions through the interface between the two regions. For this purpose, two different porous systems made of a packed bed of spheres and rectangular rods are analysed and the results are compared against a solid block case of the same size. Flow visualization shows that a significant portion of the fluid entering the porous blocks leaks from the porous region to the non-porous region through the porous-fluid interface. To discuss the effects of this flow leakage on the flow features and heat transfer, discussions are made regarding velocity, pressure, and temperature fields, as well as coherent structures, and turbulence production. The flow pattern inside the porous region indicates that the flow leakage clogs the pore channels inside the porous medium which induces a significant reduction in the streamwise momentum of the pore flow. In addition, coherent structures show that flow leakage leads to the creation of counter-rotating vortex pairs of fluid flow within and above the porous block that results in the formation of organized hairpin structures. Finally, the comparison of turbulence production for the porous and solid cases together with the onset growth of the Kelvin-Helmholtz instability on the porous-fluid interface show a reduction in turbulent kinetic energy above the leading edge of porous blocks. This observation implies that for the porous cases the transition to turbulence is postponed to the downstream of the porous block and it is not achieved as fast as the solid block.

1. Introduction

Porous materials have many applications in heat transfer enhancement including fuel cells [1,2], heat sinks for electronics cooling [3–7], heat exchangers [8–10], flow and heat transfer control [11], transpiration cooling [12], convective drying [13,14], packed bed [15,16], energy storage [17,18] and renewable energy [19,20]. For innovations in the design of heat management systems using porous materials, it is crucial to gain a step change in the fundamental understanding of flow and heat transfer in composite porous-fluid systems (see Fig. 1). To give a clear example, with the development of solar energy, the facilities of energy conversion from solar radiant energy to thermal energy such as solar collectors, solar receivers, and thermal energy storage facilities have been widely used to supply steam and hot water in industrial or commercial applications. As a type of low-quality energy, solar energy has a low conversion efficiency. Therefore, porous material with high thermal performance is utilized to improve the efficiency of solar facilities [19,21]. Or as another example, in aerospace engineering and

electronic production cooling, the heat exchangers demand lighting, compactness and effectiveness. Recent findings show that compact heat exchangers embedded with porous material that is developed based on a composite porous-fluid system with an optimized blockage ratio in the heat transfer region are an efficient method to improve the heat exchanger performance [22,23].

A composite porous-fluid system is shown in Fig. 1 which is divided into the porous and non-porous regions (or clear flow region) separated by an interface—called a porous-fluid interface. The exchange of heat and flow between the porous and non-porous regions in a composite porous-fluid system is gaining expanding academic and industrial attention [24–28]. It has been shown that partial blockage of the flow area adds another unknown to the problem: ‘the interface modelling of a porous and non-porous region’ [29–31]. While physically one expects much lower fluid velocity in the pores compared to that of free flow, capturing this sharp gradient at the interface can add to the difficulties of the numerical simulation. Beavers and Joseph [32] were amongst the first to show that sharp gradients at the interface between the porous and fluid regions exist. Their work highlighted the existence of a slip velocity at

* Corresponding author.

E-mail address: yasser.mahmoudilarimi@manchester.ac.uk (Y. Mahmoudi).

Nomenclature		Symbol
D	Sphere diameter (distance between the centres of two consecutive pores)[m]	$\theta = \frac{(T-T_s)}{(T_{in}-T_s)}$ Dimensionless temperature [–]
f	Frequency[Hz]	ρ Density [kg/m ³]
h_r	Height of secondary recirculation region in front of windward face[m]	$\sigma_u = u'/u_{RMS}$ Normalized streamwise fluctuation[–]
H_r	Height of primary recirculation region over the interface [m]	$\sigma_v = v'/v_{RMS}$ Normalized vertical fluctuation[–]
K	Permeability [m ²]	ν Molecular kinematic viscosity [m ² /s]
k	Turbulence kinetic energy[m ² /s ²]	ν_{SGS} Sub-grid scale eddy viscosity[m ² /s]
l_r	Length of secondary recirculation region in front of windward face[m]	Φ Porosity [–]
L_r	Length of primary recirculation region over the interface [m]	ω Vorticity [1/s]
LW_r	Length of recirculation region in the wake region[m]	Ω_{ij} Rotation rate tensor [1/s]
p	Pressure[Pa]	Δ Filter width [m]
P_k	Turbulence production[m ² /s ³]	$\langle \dots \rangle$ Time-averaged value [–]
Q	Second invariant of velocity gradient tensor[1/s ²]	
$Re = UD/\nu$	Reynolds number[–]	
S_{ij}	Strain rate tensor[1/s]	
Δt	Time step[s]	
t	Time[s]	
$t^* = t \times U/D$	Non-dimensional time unit[–]	
T	Temperature[K]	
u	Streamwise velocity component[m/s]	
U	Inlet velocity[m/s]	
v	Vertical velocity component[m/s]	
X	Streamwise direction[m]	
Y	Vertical direction[m]	
Z	Lateral direction[m]	

Subscript	
in	Inlet
Exp	Experimental
Num	Numerical
r	Recirculation
res	Resolved
RMS	Root mean square
s	Sphere wall/surface
SGS	Sub-grid scale
solid	Solid block

Superscript	
-	Filtered
'	Fluctuation

Abbreviation	
CFL	Courant–Friedrichs–Lewy number [–]
TKE	Turbulent kinetic energy [m ² /s ²]

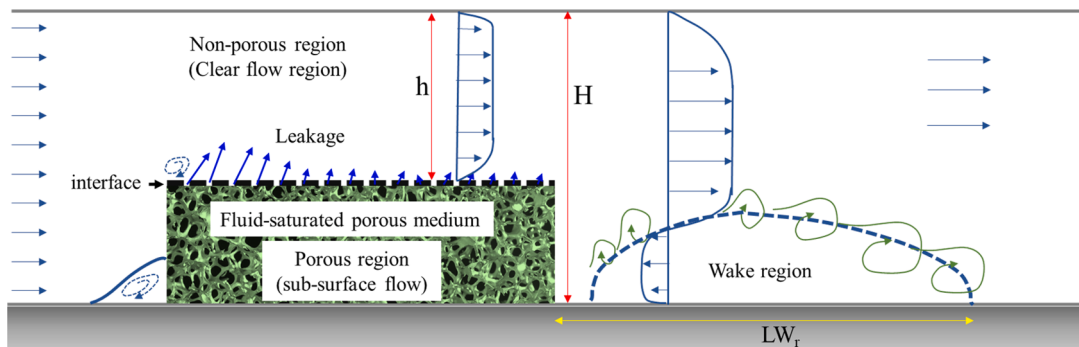


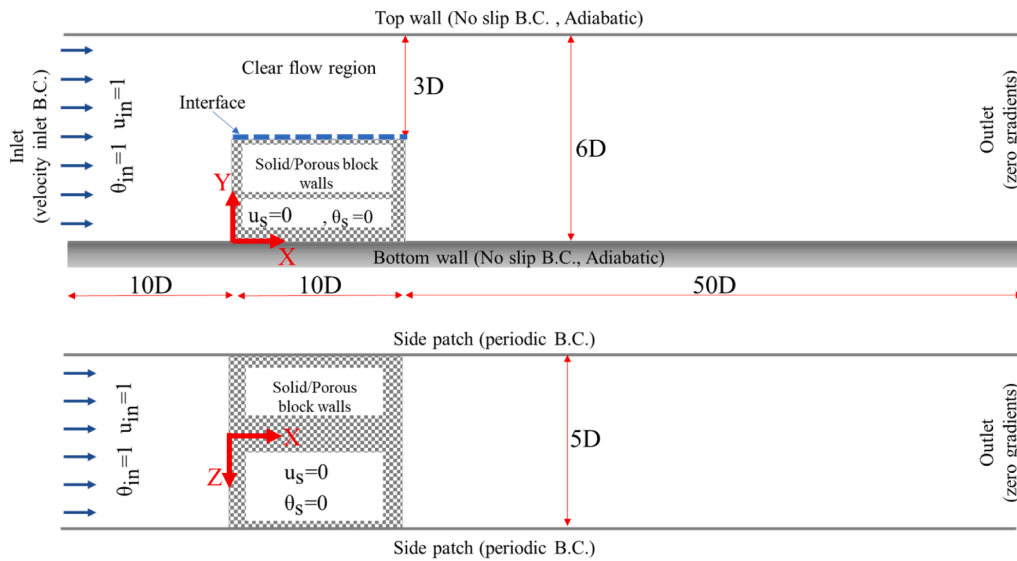
Fig. 1. Flow over a porous medium in a channel (composite porous-fluid system) showing a schematic of flow leakage from the interface.

the interface. From there, authors have established different interface conditions that can be classified into two main types according to Alazmi and Vafai [33]: slip and no-slip boundary conditions. Those authors then establish five main categories for the hydrodynamic interface conditions that they critically examined. Moreover, the validity of Local Thermal Equilibrium (LTE) has been studied extensively in a channel partially filled with porous media [34–38]. Mahmoudi, et al. [34] investigated the effect of different parameters such as inertia parameter (F), Darcy number (Da), solid to fluid conductivity ratio, porosity, porous layer thickness and particle diameter on the validity of LTE in porous media. They found the optimum radius of porous material that up to which the LTE holds. Forooghi, et al. [35] investigated the steady and pulsatile flow and heat transfer in a channel lined with two porous layers subject to constant wall heat flux under Local Thermal Non-Equilibrium (LTNE)

condition. It was observed that the Nusselt number inside the channel increases when the problem is tending to the LTE condition. Therefore, careless consideration of LTE may lead to an overestimation of heat transfer.

Recent experimental studies [27,39] show that in a composite porous-fluid system, for some certain blockage ratios and pore density, the fluid in the porous region is pushed away from the foam into the non-porous region on the top of the foam block before reaching the foam end (flow leakage). Flow leakage introduces a new challenge for modelling heat and fluid flow in porous media to account for the exchange of flow properties at the interface.

Despite the clear relevance and importance of composite porous-fluid systems to a wide range of applications, the problem of fluid flow and heat transfer in such systems has not been fully resolved. In



a) Front and top view of the computational domain, u is the velocity and θ is the dimensionless temperature.

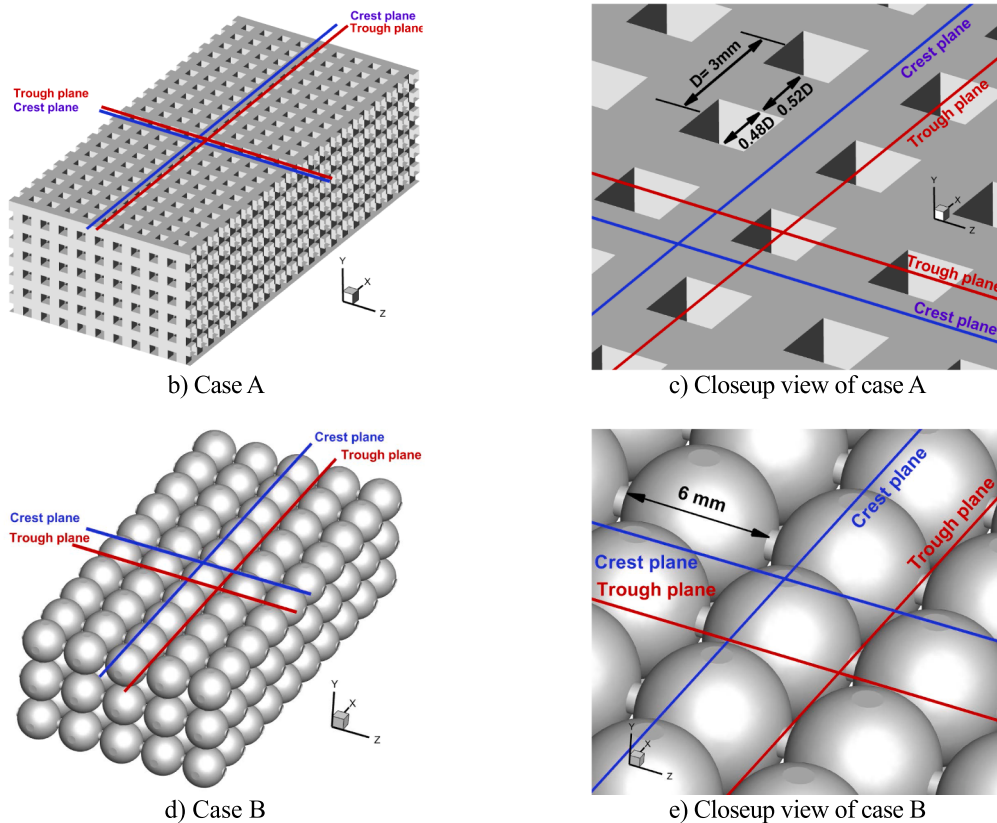


Fig. 2. a: Computational domain and boundary conditions; b: Porous block formed from rectangular cross-section ($0.52D \times 0.52D$) ligament with a smooth interface and porosity 48%; c: Closeup view of porous block for case A; d: Porous block with cubic packed arrangement formed from spheres with a rough interface (bridge method is employed at the contact point of spheres, porosity 53%, $D = 6\text{ mm}$); e: Closeup view of porous block for case A; Red and blue lines: Illustration of two spanwise and streamwise locations for presenting results, the red line lies over the “trough plane” and the blue line lies over the “crest plane”.

addition, the mechanism of energy and momentum transportation across the interface is still not fully understood. Especially, when the porous block leads to the formation of stagnation, recirculation, and wakes in the channel flow and the flow leaks from the porous region to the non-porous region. Tackling this problem requires an in-depth understanding of the linkage between these two flow regimes at the pore level. This study aims to use large eddy simulations (LES) to obtain new

information on the fluid flow and heat transfer between the porous and non-porous regions and to address the connection between these two regions. For this purpose, a composite porous-fluid system is investigated using pore-scale LES analysis where the complete flow field is resolved in the non-porous region and within the pores of the porous region. The findings of this study are insightful for the community in this field to develop proper momentum and thermal boundary conditions at

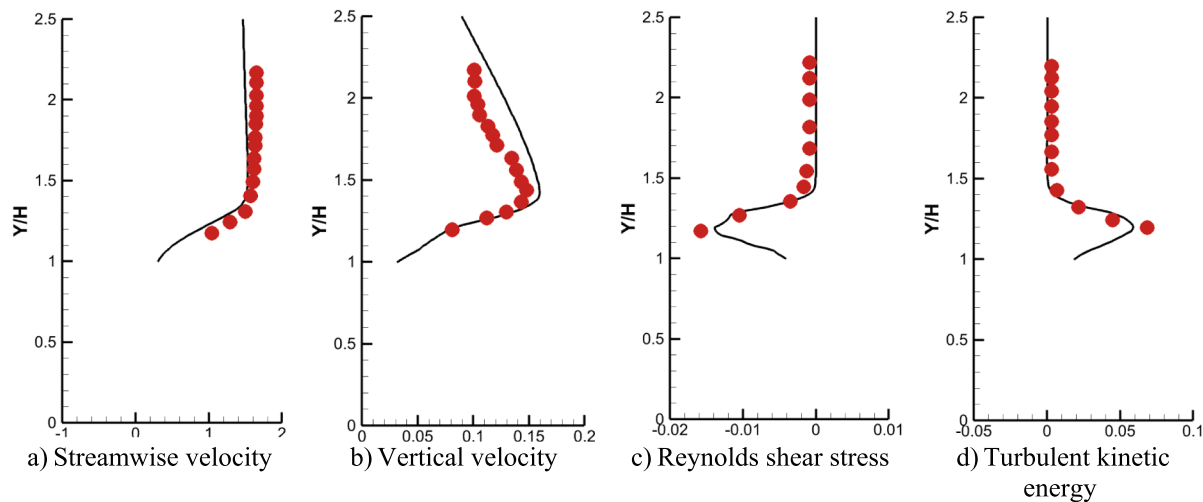


Fig. 3. Comparison of velocity profiles, Reynold shear stress $\langle u'v' \rangle/U^2$ and turbulent kinetic energy TKE = $0.5(\overline{u'^2} + \overline{v'^2} + \overline{w'^2})$ obtained from the present LES study (solid lines), against the experimental data (symbols) [50] above the porous interface at $X/H = 1.6$.

the porous-fluid interface which has been a challenging question for more than four decades [32–34,40]. Moreover, the present study could provide a key to understanding flow physics inside and over the porous material based on the pore-scale LES. Because access to detailed flow measurement using an experimental approach is quite challenging due to the pore-scale constraints in the porous media, and the numerical approach based on the volume average method is not capable to visualize the flow physics in the pores.

2. Computational methodology

2.1. Computational domain & boundary condition

The computational domain is a 3-dimensional porous medium in a channel wherein a porous block is inserted in the channel as depicted in Fig. 2. Three different porous cases are studied (1) packed bed made of rectangular cross-section ligaments with a smooth interface, Fig. 2(b); (2) packed bed made of spheres with diameter D—Fig. 2(c); and (3) is a porous block with the permeability of zero (i.e. solid block) shown in Fig. 2(d). These porous structures impose two different interface surface topographies, namely: a smooth and rough interface that make the arguments more general. The blockage ratio (i.e., the ratio of the height of the porous region to the channel height) is 0.5 in all cases. The computational domain has the dimensions of 70D, 6D, and 5D in the X, Y, and Z directions, respectively. The flow Reynolds number based on the channel height and inlet velocity is 3600. Permeability estimation is performed utilising $K = \Phi^3 D_p^2 / 180(1 - \Phi^2)$ [41,42] where, $D_p = 6V_p/A_p$ is the mean particle diameter with V_p the volume and A_p the surface area of the solid obstacles. This equation gives $K = 3.65 \times 10^{-8} \text{ m}^2$ and $7.19 \times 10^{-9} \text{ m}^2$ for cases A and B, respectively.

In Fig. 2 the details of boundary conditions are depicted. No-slip boundary condition is considered on the solid surface in the porous region. Constant wall temperature boundary condition (i.e., $\theta = 1$) is applied on the solid surfaces of the porous region. The bottom and top boundaries of the channel are assumed adiabatic. Moreover, two spanwise and streamwise locations for the porous blocks where LES results are presented and discussed, namely: “trough plane” and “crest plane” are shown in Fig. 2. At these two locations, both porous blocks for cases A and B possess very different boundary conditions along the interface owing to the presence of permeability. The interface on the crest plane is locally impermeable, allowing no flow penetration at this location. Nonetheless, the trough plane has a fully open (permeable) interface, which enables fluid exchange between the surface and subsurface

regions.

2.2. Numerical method

The LES filtered equations are acquired as in Eqs. (1) – (3):

$$\frac{\partial \bar{u}_i}{\partial x_i} = 0 \quad (1)$$

$$\frac{\partial \bar{u}_i}{\partial t} + \frac{\partial}{\partial x_j} (\bar{u}_i \bar{u}_j) = -\frac{1}{\rho} \frac{\partial \bar{p}}{\partial x_i} + \frac{\partial}{\partial x_j} \left(\left(\nu + \nu_{SGS} \right) \frac{\partial \bar{u}_i}{\partial x_j} \right) \quad (2)$$

$$\frac{\partial \bar{T}}{\partial t} + \frac{\partial}{\partial x_j} (\bar{T} \bar{u}_j) = \frac{\partial}{\partial x_j} \left(\left(\alpha + \alpha_{SGS} \right) \frac{\partial \bar{T}}{\partial x_j} \right) \quad (3)$$

where \bar{u}_i , \bar{p} and \bar{T} are the filtered velocity in i th direction, the pressure and temperature respectively [43]. The filter function is taken as a simple box filter, Δ , with filter width equal to the cube root of cell volume. In the present study, the ν_{SGS} is modelled using the dynamic SGS turbulent kinetic energy model [44]. In addition, α_{SGS} is related to the ν_{SGS} through the SGS Prandtl number, $Pr_{SGS} = \nu_{SGS}/\alpha_{SGS}$, which is assumed 0.7 in this study [45]. The filtered governing equations are discretized by implementing the finite volume method. All the computations are carried out in the OpenFOAM CFD package [46]. The second-order central difference scheme is adopted for spatial discretization. The implicit second-order backward difference scheme is used for the time integration. The PISO is taken on for the pressure–velocity coupling in all the present simulations [47]. To accurately capture the evolution of the flow features, the physical time step is chosen for each grid such that the CFL number is kept below unity. Time averaging process is begun when the initial transient conditions are washed out and a semi-steady state operating condition is reached. All the present numerical results are averaged over a period of 490 non-dimensional time units ($t^* = t \times U/D$), where U is the flow mean velocity at the channel inlet. The computational domain is discretized into 10.5 million non-uniform cells with a minimum grid spacing of 0.01D in the X, Y, and Z directions. The grid resolution is assessed based on the two-point correlation and integral length scales [48]. It is found that at least 6 cells have been included in the vertical integral length scale at the center plane ($Z/D = 0$) at $X/D = 12$ seeming to be sufficient [49].

2.3. Validation

In porous media systems, local on-site measurements of the flow

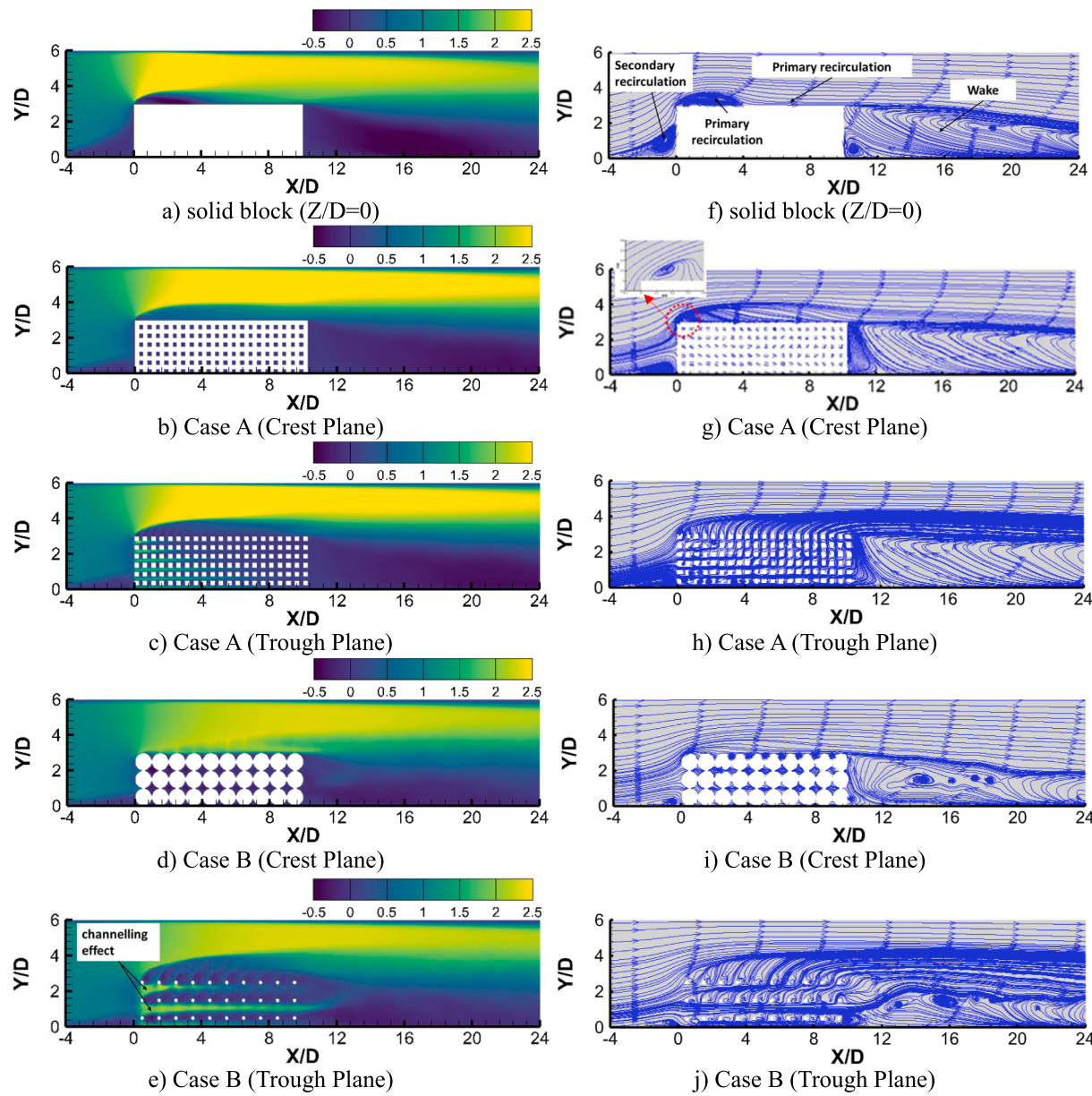


Fig. 4. Left: Contours of time-averaged streamwise velocity for the porous Cases A and B and C; Right: Flow field within and above the porous blocks illustrated by streamlines.

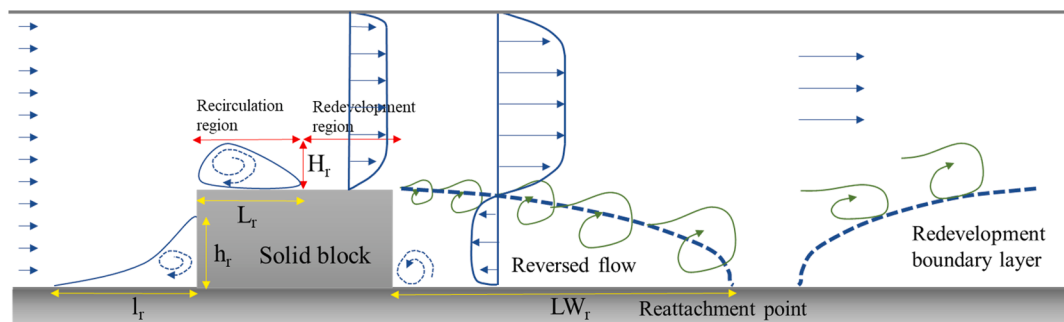


Fig. 5. Schematic flow features of the solid block case.

properties (e.g., temperature and velocity) are very difficult due to the small and complex flow passage within the pores. Specifically, temperature measurement using intrusive techniques (e.g., thermocouples)

disturbs the fluid flow and thus causes a substantial error in the data recorded. Therefore, the existing experimental studies in composite porous-fluid systems are limited to some velocity data in the porous

Table 1

Dimensions of the primary and secondary recirculation together with the reattachment length in the wake region for three cases A, B and C.

	l_r / D	h_r / D	L_r / D	H_r / D	LW_r / D
Solid block	4.53	1.78	4.19	0.47	20.11
Case A (crest plane)	3.75	0.44	0.30	0.15	25.65
Case A (trough plane)	3.66	0.44	–	–	25.60
Case B (crest plane)	3.04	0.29	–	–	24.93
Case B (trough plane)	2.68	0.28	–	–	24.72

region. The developed LES solver has been validated with respect to the experimental data of Leu, et al. [50]. They measured flow velocity components and turbulence statistics in a channel with a porous block mounted on the bottom wall. The porous block consisted of glass beads, having diameters ($D = 0.015$ m) that were arranged in a non-staggered pattern with a porosity of 47.5%. The length (L), width (W), and height (H) of the block are 0.15 m, 0.3 m and 0.075 m, respectively. The porous block has been mounted at a position of $40H$ downstream of the inlet. Since the distance between the block and the inlet is very long and computationally expensive for LES. Hence, to reduce computational time, in the present study it is reduced to $4H$ and the Divergence-Free Synthetic Eddy Method [51] is utilised based on a full domain RANS input data for inflow turbulence generation at this location. Fig. 3 compares the present LES results and experimental data for streamwise and vertical velocity components, Reynolds shear stress and turbulent kinetic energy above the porous block at $X/H = 1.6$. The figure shows that the developed LES model can predict well the experimental data at locations above the porous block and in the wake downstream of the

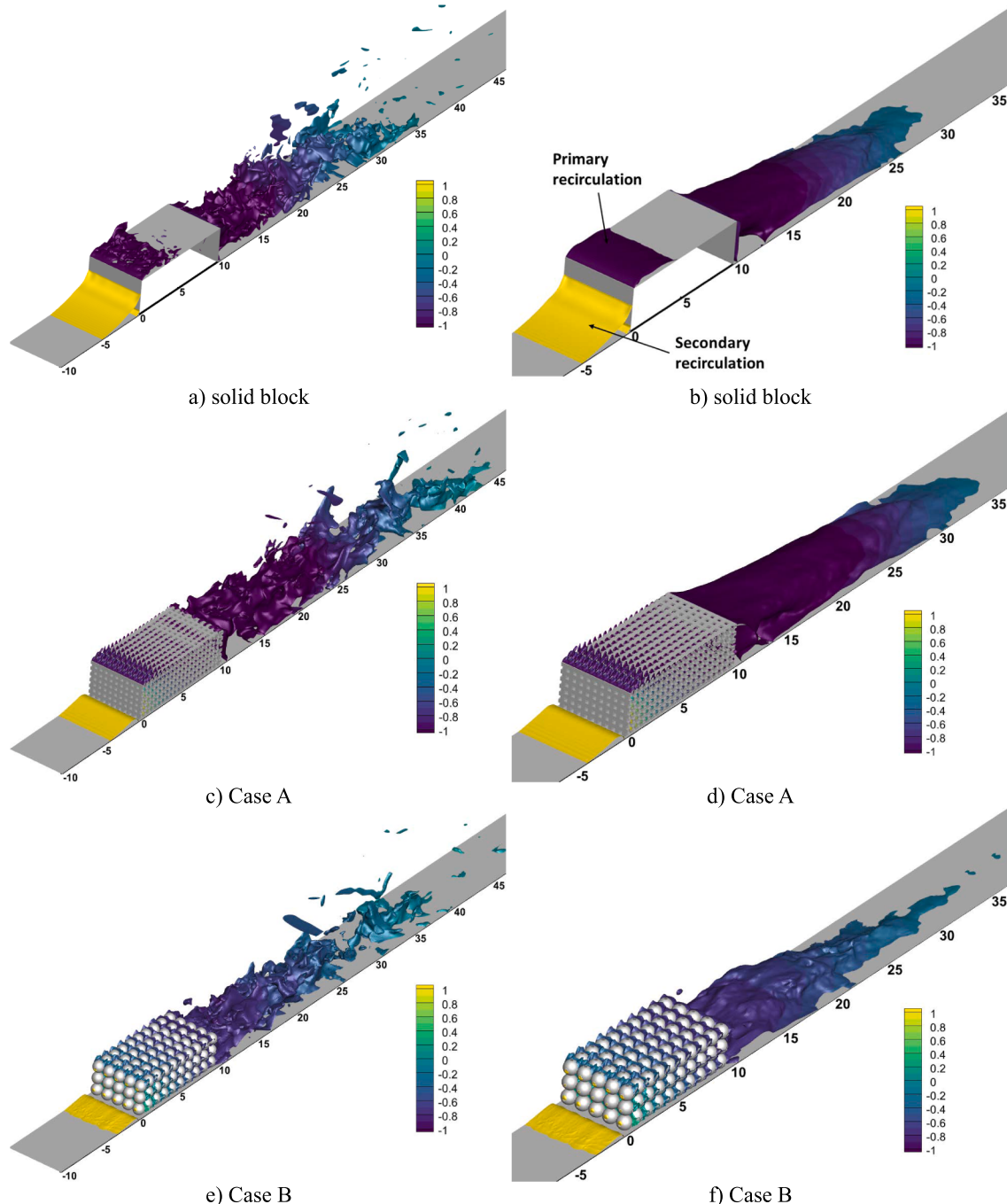


Fig. 6. Left: Instantaneous iso-surface of zero streamwise velocity ($\bar{u} = 0$); Right: Time-averaged iso-surface of zero streamwise velocity ($\langle u \rangle = 0$).

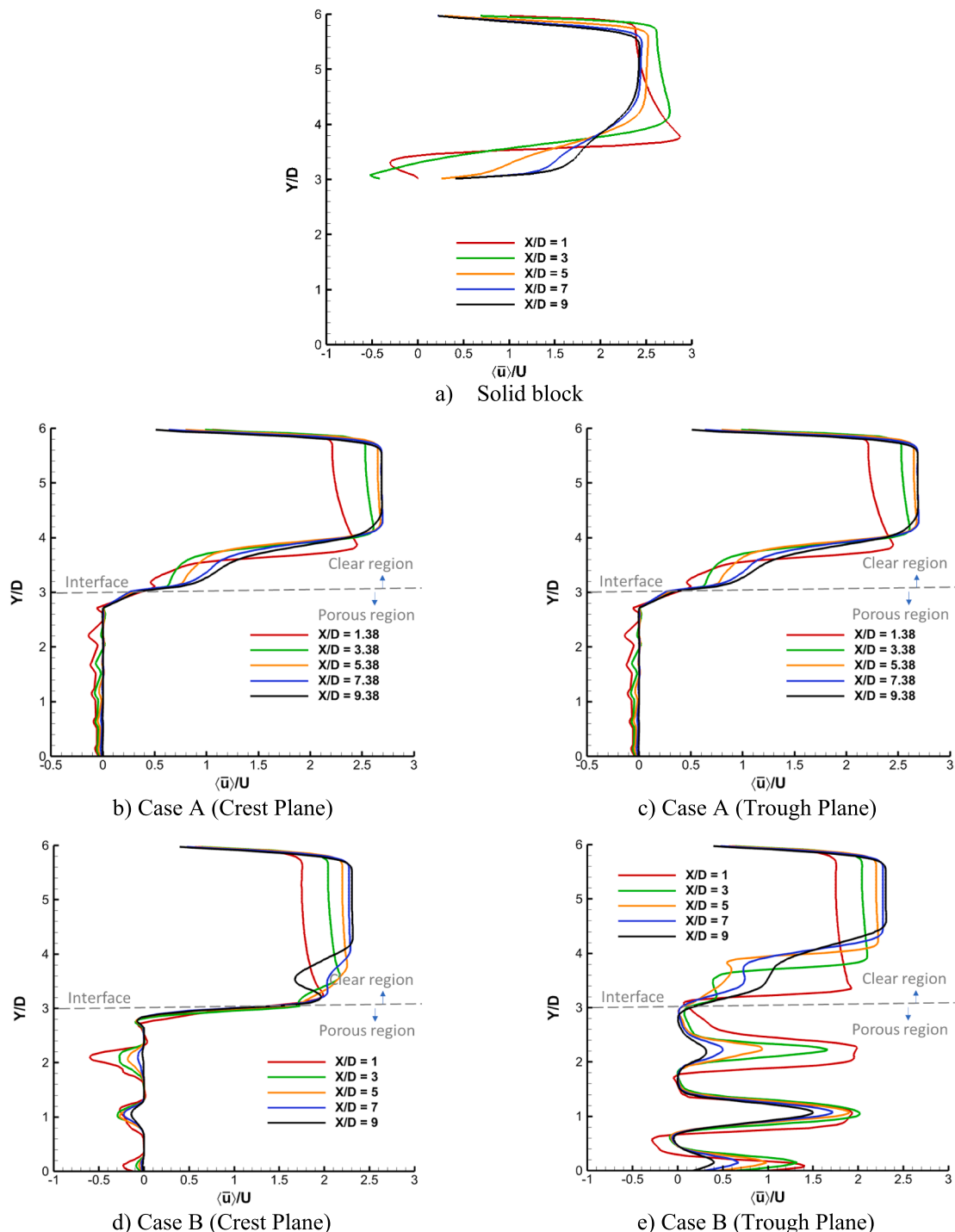


Fig. 7. Vertical distributions of time-averaged streamwise velocity at different streamwise locations along the porous block.

porous block. The slight discrepancy observed in Fig. 3 is attributed to the RANS input data employed for the LES inflow turbulence generation.

3. Discussion of results

3.1. Flow field

3.1.1. Streamwise velocity

Contours of time-averaged streamwise velocity on the crest and trough planes for the three different cases, A, B and C (see Fig. 2) are presented in Fig. 4. The velocity fields are very different for the three

cases. The main flow patterns for the solid block are classified as 1) boundary layer development region in front of the block; 2) flow separation and recirculation region in front of the block; 3) flow recirculation and reattachment region; 4) boundary layer redevelopment region on the top wall of the block; and 5) flow separation and recirculation region downstream of the block in the wake (Fig. 5). The first separation, which is triggered by an adverse pressure gradient caused by blockage of the solid block, occurs at a distance l_r upstream of the leading edge of the solid block and reattaches on the windward face of the block at a distance h_r above the floor. The second detachment occurs at the leading edge of the block and reattaches at a distance L_r downstream of the

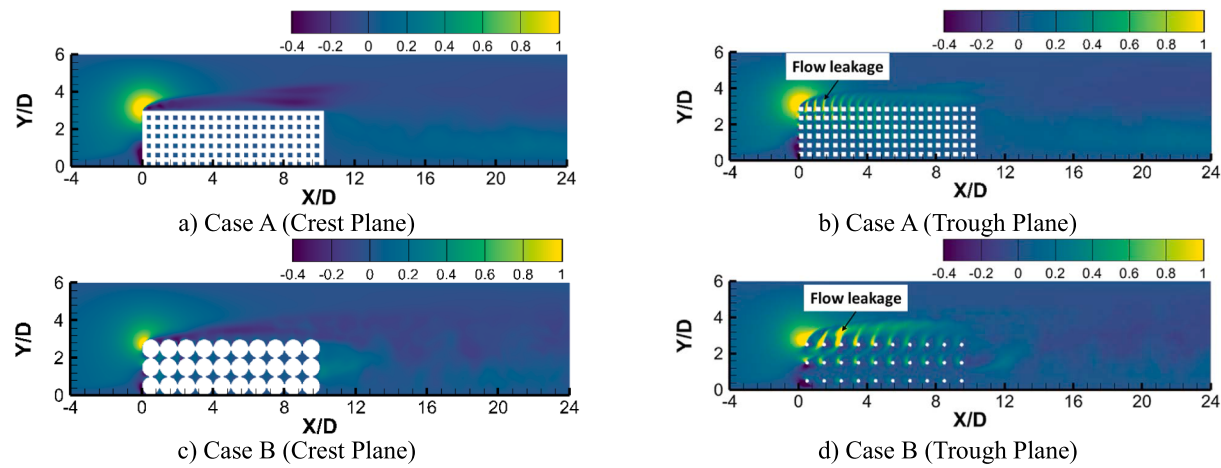


Fig. 8. Left: Contours of time-averaged vertical velocity for the porous cases A and B.

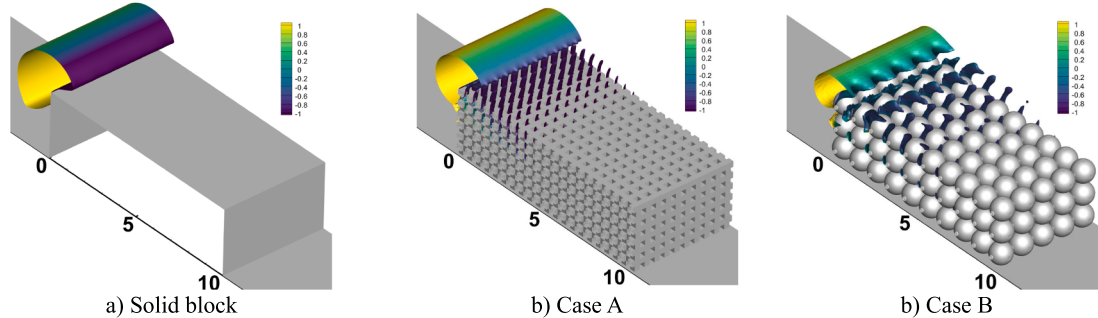


Fig. 9. Three-dimensional representation of the flow leakage from the porous block by iso-surface of vertical velocity ($|v|/U = 0.5$) coloured by time-averaged pressure.

Table 2
Absolute and relative values of flow rate that leaks from the porous blocks.

	Position X along the interface	Case A	Case B
$Q_{in} \times 10^4$ [m ³ /s]		1.4	2.7
$Q_{IX}/Q_{in} \times 100$	X = 2.5D	47.9	52.8
$Q_{IX}/Q_{in} \times 100$	X = 5.0D	74.1	64.8
$Q_{IX}/Q_{in} \times 100$	X = 7.5D	91.4	75.4

leading edge of the block. The maximum height of the second recirculation region is denoted by H_r . Finally, the redevelopment boundary layer on the top surface gets detached at the trailing edge of the solid block and reattaches at a distance LW_r downstream of the leeward face and forms the wake region. The size of primary and secondary recirculation together with reattachment length in the wake region are listed in Table 1. However, in the case of a porous block, the flow is allowed to penetrate the void spaces (pores) of the porous block and the size of both l_r and h_r of the secondary recirculation region in front of the windward face is reduced considerably (see Table 1). In addition, the reverse flow pattern along the interface is not observed on the trough plane; on the crest plane, it is insignificant and restricted to the very small area adjacent to the leading edge of porous blocks (see Table 1 and Fig. 4 (g, i)).

Below the interface in the porous region, the mean streamwise velocity shows distinct flow behaviour in Fig. 4. The channelling effect dominates the flow pattern in the trough plane, thus producing streamwise-oriented high-momentum paths in the horizontal direction (see Fig. 4(c, e)). In addition, the mean streamwise momentum increases as one moves toward the bottom of the porous block and decreases meaningfully in the upper layer of the porous.

Time-averaged and instantaneous iso-surfaces of $\bar{u} = 0$ are represented in Fig. 6 to have a better insight into the formation of primary and secondary recirculation regions and the downstream wake flow. The figures show that for all cases, there exists a recirculation region downstream of the blocks. For the porous cases, however, the reattachment point moves downstream due to the fluid flow exiting from the pores on the leeward face of the porous block as can be noticed in Fig. 4 (h, j). Inspection of the flow reattachment region behind the porous blocks reveals a large reverse flow zone for both porous blocks compared to the solid block case. The reattachment length (LW_r) in the wake region at the symmetry plane ($Z/D = 0$) is 127% and 123% for case A and case B, respectively longer than that in the solid block case.

Fig. 6 shows that flow leakage (see Section 3.1.2) destroys the strong reverse flow pattern of the primary recirculation region into a small local reverse flow pattern (see Table 1). Moreover, the flow penetration into the void spaces significantly shrinks the size of the secondary recirculation region in front of the windward face for the porous blocks.

Vertical distributions of time-averaged streamwise velocity through and above the porous region have been compared with the solid block case in Fig. 7. The strong negative streamwise velocity in Fig. 7(a) confirms the presence of a primary recirculation region for the solid block while this reverse flow is not observed above the interface for the porous cases. This observation confirms the deterioration of reverse flow above the interface for the porous cases as discussed previously in Fig. 6. Below the interface in the porous region, the velocity profiles have a non-uniform wavy shape due to the geometric characteristics of the pores and they continuously experience acceleration and deceleration due to contractions and expansions of the flow as they pass through the pores. Moreover, Fig. 7(c, e) shows a drop in the maximums of streamwise velocity below the interface on the trough plane. For

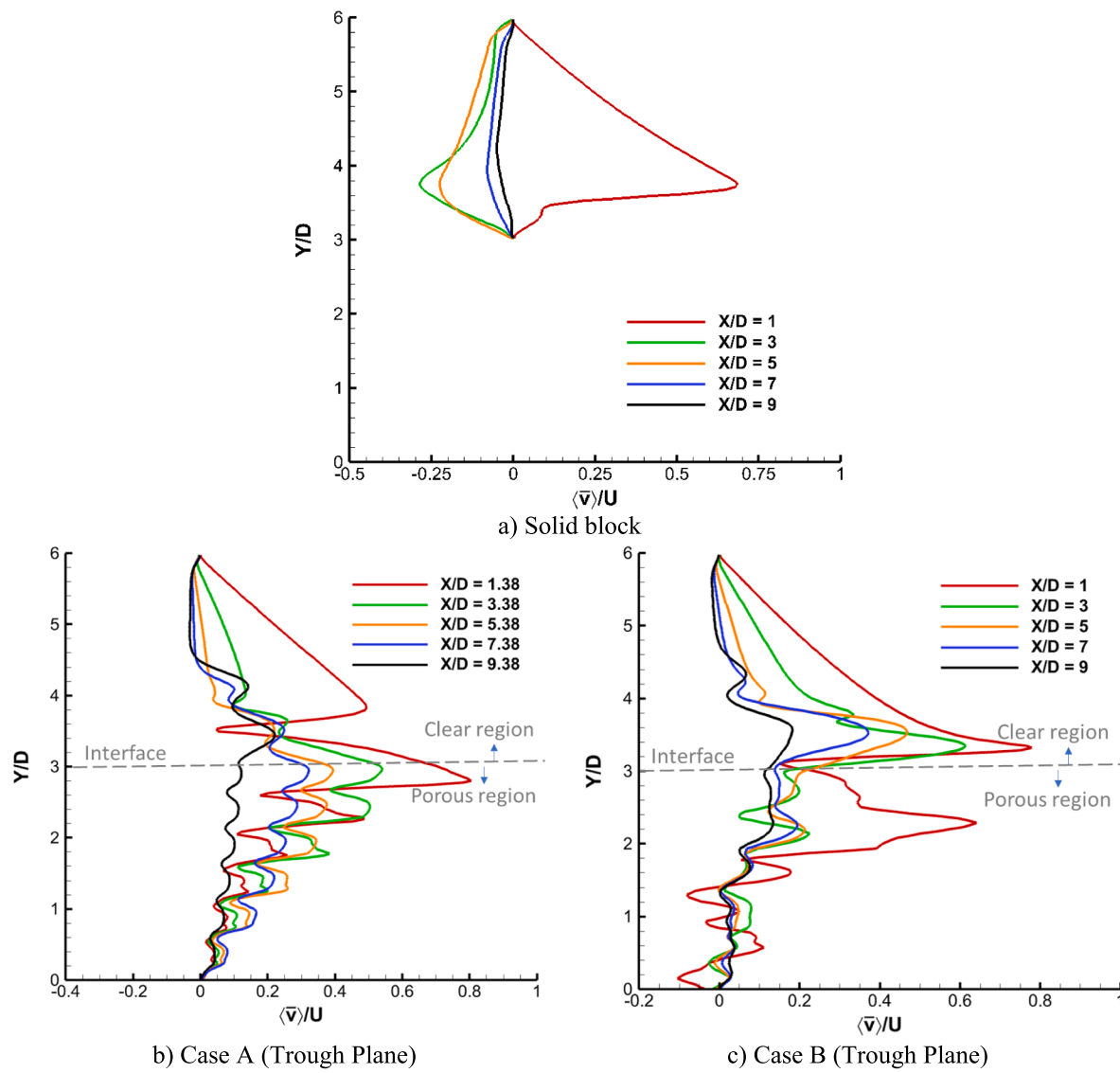


Fig. 10. Vertical distributions of time-averaged vertical velocity at different streamwise locations along the porous block.

example, for case A the mean streamwise velocity is lowest in magnitude between $2.5 < Y/D < 3$. This observation challenges the classic notion of a monotonic mean velocity decrease, which is well-established for laminar flow [52].

3.1.2. Vertical velocity

Fig. 8 shows the contours of time-averaged vertical velocity on the crest and trough planes. The very first visible feature is that some portion of the fluid entering the porous blocks is pushed upwards toward the porous-fluid interface and leaves the porous region to the non-porous region (flow leakage). This phenomenon is represented by the positive iso-surface of time-averaged vertical velocity in Fig. 9. Moreover, the contours of the mean vertical velocity at the trough region in Fig. 8 (b, d) clearly show that vertical penetrating flows clog the horizontal channels inside the porous block which induces a significant reduction in streamwise momentum of the pore flow, especially at higher porous levels near the interface as discussed in Fig. 7 and Fig. 4.

The time-averaged value of flow rate that enters the porous block from the windward face, Q_{in} and leaks from the porous block, Q_{IX} (X is the axial position along the porous-fluid interface from the leading edge of the porous region) are calculated using the following equations:

$$Q_{in} = \int_0^{3D} \int_{-2.5D}^{2.5D} u(Y, Z) dZ dY \quad (4)$$

$$Q_{IX} = \int_0^X \int_{-2.5D}^{2.5D} v(X, Z) dZ dX \quad (5)$$

Table 2 shows that more than half of the flow entering the porous block leaks from the porous region before $X/D = 5$. Comparison of flow leakage for cases A and B shows that for case B with higher permeability, nearly 75% of entering flow leaks before $X/D = 7.5$, whereas this value is more than 91% for case A with lower permeability. This observation indicates the higher tendency of flow leakage in porous media with lower permeability. This further explains the higher clogging of horizontal channels inside the porous block observed in Fig. 4 for case A.

Vertical distributions of time-averaged vertical velocity through and above the porous region for cases A and B are shown in Fig. 10. The non-uniform wavy shape of the streamwise velocity profile is also repeated in this figure within the porous block. However, contrary to Fig. 7, below the interface, the mean vertical velocity is nearly the highest in magnitude. In addition, there is a constant increase in maximum values of vertical velocity toward the interface. This behaviour of vertical velocity confirms the flow leakage and strong interaction between the

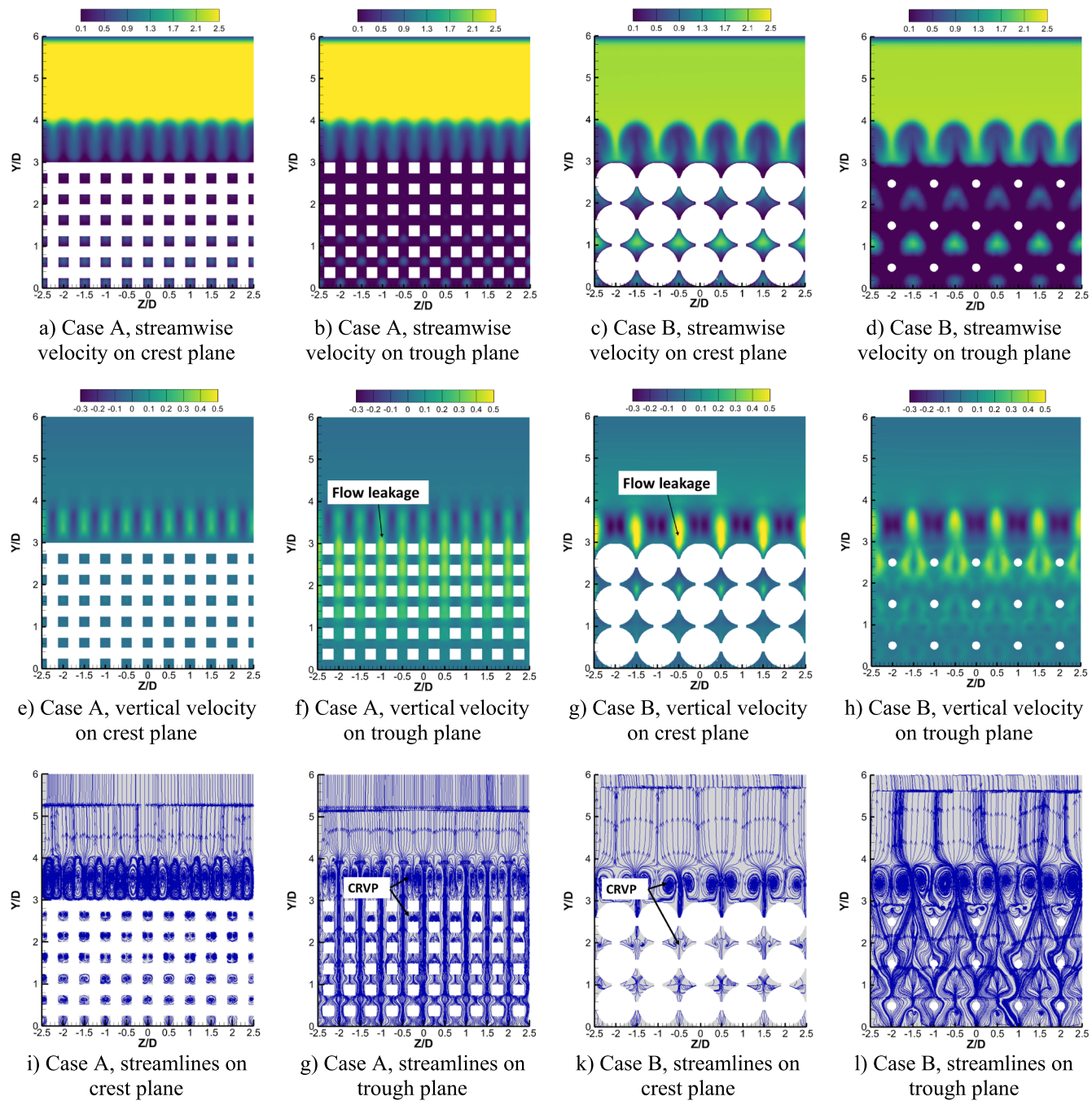


Fig. 11. Side view contours of time-averaged; Row 1: streamwise velocity; Row 2: vertical velocity; Row 3: streamlines Column 1: case A, crest plane; Column 2: case A, trough plane; Column 3: case B, crest plane; Column 4: case B, trough plane.

porous and non-porous regions at the interface previously discussed in Fig. 7 and Fig. 9.

As argued in Fig. 7 the mean streamwise component of velocity just underneath the interface is lower than that at the deeper layers. The most compelling theory for this unexpected behaviour is flow leakage. Positive values of vertical velocity on the trough planes indicate that the leakage from the porous region to the non-porous region is the main reason for modifications of the flow close to the interface; It also confirms the pore-flow streamwise momentum loss just below the interface.

3.1.3. Counter-rotating vortex pairs

Side view contours of streamwise velocity components for the two porous block cases are shown in Fig. 11(row 1). Streamwise velocity illustrates the channelling effect producing high-momentum paths in the

streamwise direction. As discussed before, the magnitude of streamwise pore flow is reduced below the interface due to the flow clogging by flow leakage. Fig. 11(row 1) shows that the time-averaged streamwise momentum decreases in the upper layer of the porous blocks. The vertical velocity in Fig. 11(row 2) shows an upward tendency of the flow inside the porous region that passes through the porous pores and penetrates to the clear region (flow leakage). Streamlines in Fig. 11(row 3) show the presence of organized counter-rotating vortex pairs (CRVPs) of fluid flow within and above the porous blocks. It is seen that the CRVPs for both porous structures originate from the bottom of the porous blocks and move toward the interface. In the porous region, the size of the pores limits the extent of the CRVPs; however, above the interface, they are free to expand.

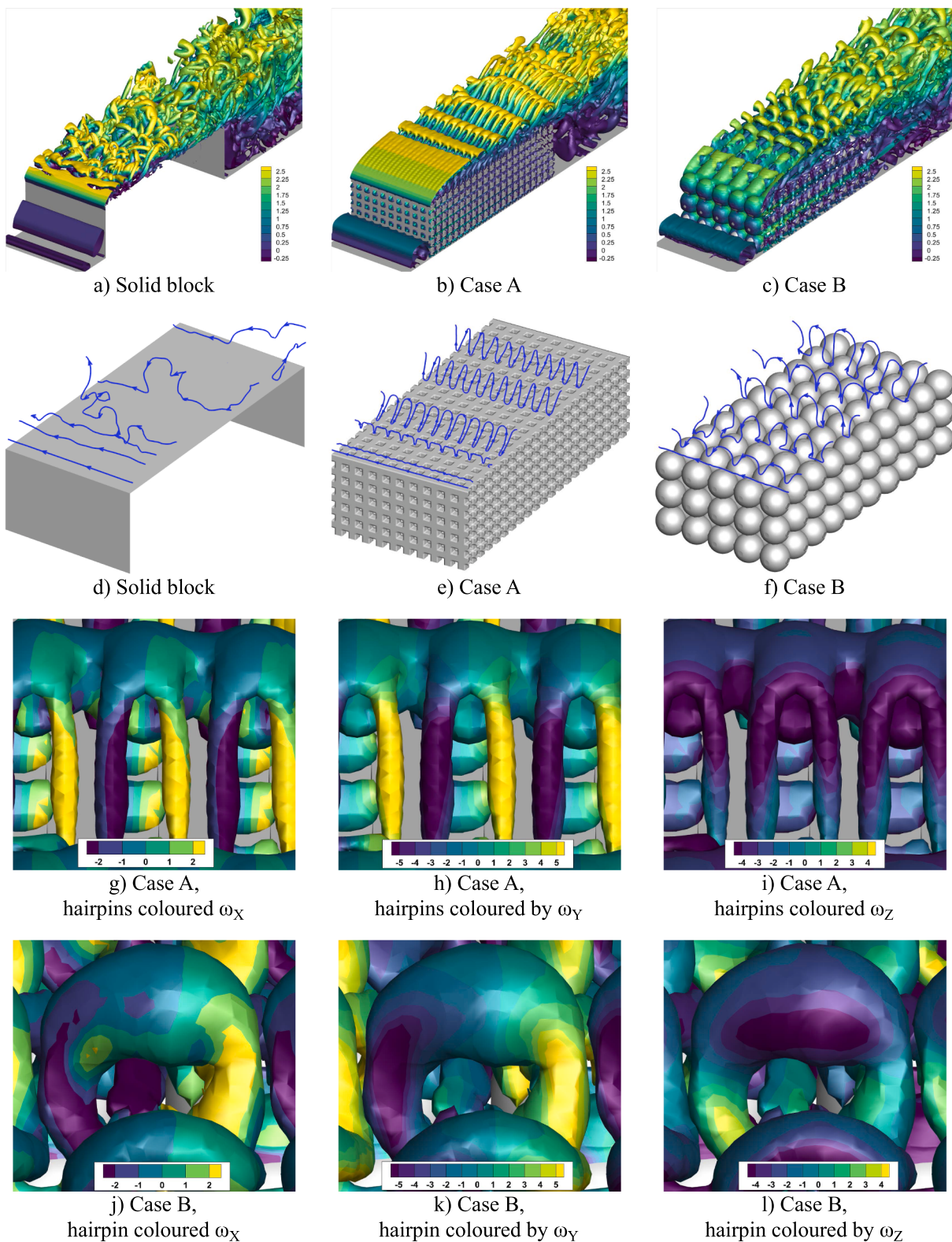


Fig. 12. Three-dimensional hairpin coherent structures identified by instantaneous iso-surface of Q-criterion ($Q = 30000 \text{ s}^{-2}$); Row 1: Coherent structures coloured by mean streamwise velocity; Row 2: Evolution of the hairpin coherent structures by vorticity lines; Row 3: Close up view of hairpins coloured by vorticity compounds for case A; Row 4: Close up view of hairpins coloured by vorticity compounds for case B.

3.1.4. Hairpin coherent structures

The flow structures for the three cases are shown in Fig. 12. The forest of vortices with a clear hairpin structure is observed over the interface in all cases (Fig. 12 (a-c)). However, the hairpin structures are not well-organised in the solid block case as opposed to the porous cases.

The evolution of the hairpin structures in Fig. 12 (d-f) shows that after the leading edge, the shear layer for all cases rolls up in a circular form to generate a spanwise vortex. The vortex is then stretched by the mean shear and lifted to form a hairpin vortex. Moreover, Fig. 12 (g-l) demonstrates the sense of rotation of the leg and neck of hairpin structures

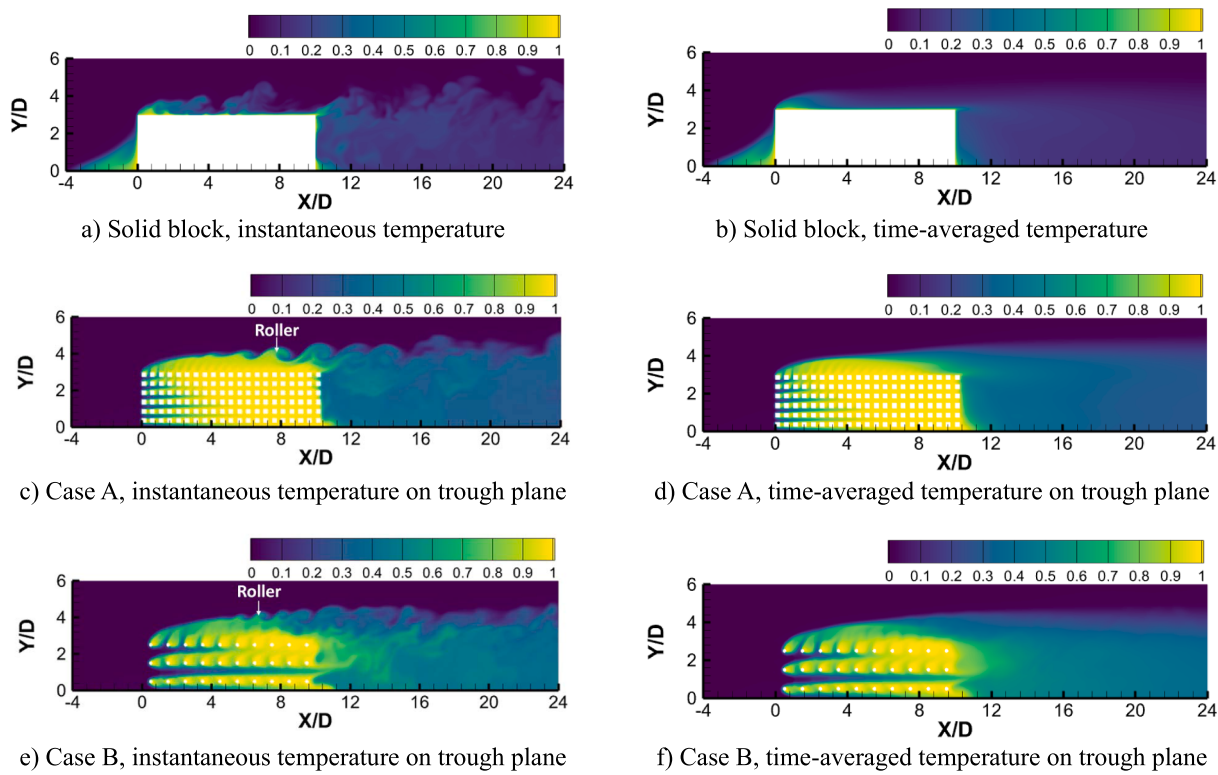


Fig. 13. Contours of Left: instantaneous temperature; Right: time-averaged temperature for the porous cases A and B.

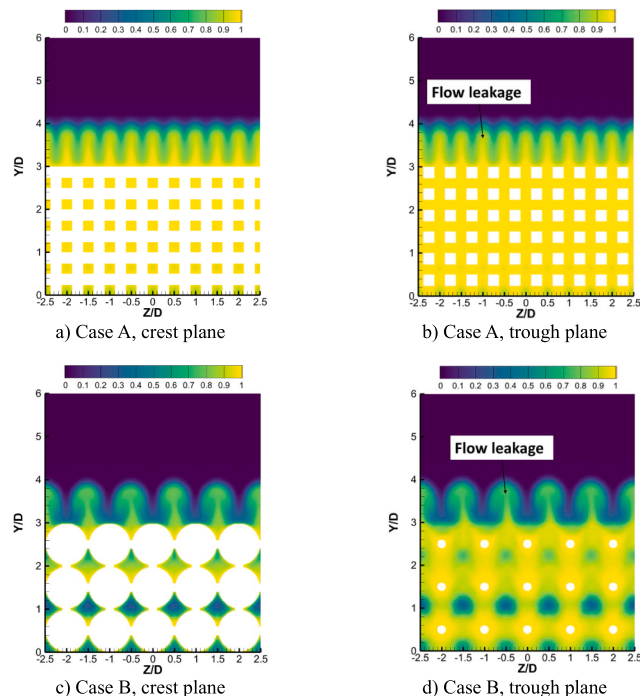


Fig. 14. Side view contours of time-averaged temperature on the crest and trough planes for cases A and B.

that are consistent with the positive and negative streamwise vorticity above the porous interface demonstrated in Fig. 11 (i-l).

3.2. Temperature field

Fig. 13 and Fig. 14 show the contours of instantaneous and time-

averaged temperature for all three cases. Fig. 13(c-f) shows that after the flow impingement on the windward face of the porous blocks, the low-temperature flow penetrates the pores of the porous block and forms high momentum channeling in the porous region. Whereas, for the solid block (Fig. 13 (a-b)) the windward face blocks the impinging flow and forms the large secondary recirculation region of high-temperature flow as previously explained in Fig. 4. Fig. 13 (a-b) confirms the presence of the primary recirculation region over the interface for the solid block where there is a strong reverse flow of high-temperature. However, no recirculation region is observed above the interface for the porous cases. For the porous block, low-temperature flow leaks from the porous region into the non-porous region on the trough planes (Fig. 13 (e-f)). This observation is more evident in Fig. 14 which further shows the evolutions of CRVPs and the entrainment of high temperature flow from the porous region to the non-porous region. Fig. 13 (c, e) show that the pattern of temperature below the interface shows the modifications of the flow close to the interface-flow leakage clogs the horizontal channels of low-temperature flow near the interface. This observation confirms the deterioration of low-temperature channeled flow in the upper layer of the porous blocks previously discussed in Fig. 10. For the porous cases, the pattern of temperature shows the growth of the shear layer above the porous-fluid interface. The evolution of the shear layer is divided into three sections. The first one is characterised by the flow separation at the leading edge of the porous block and the onset growth of the Kelvin-Helmholtz instability. The second segment is identified by vortex formation and pairing that lead to the rapid growth of the shear layer. The third segment is characterised by cross interaction of wake and shear layer that leads to the deterioration of the rollers.

3.3. Pressure field

Contour plots and vertical distributions of pressure field at different streamwise locations in the system are displayed in Fig. 15. The figure reveals a negative vertical pressure gradient inside the porous block that pushes the fluid entering the porous blocks upwards to the non-porous

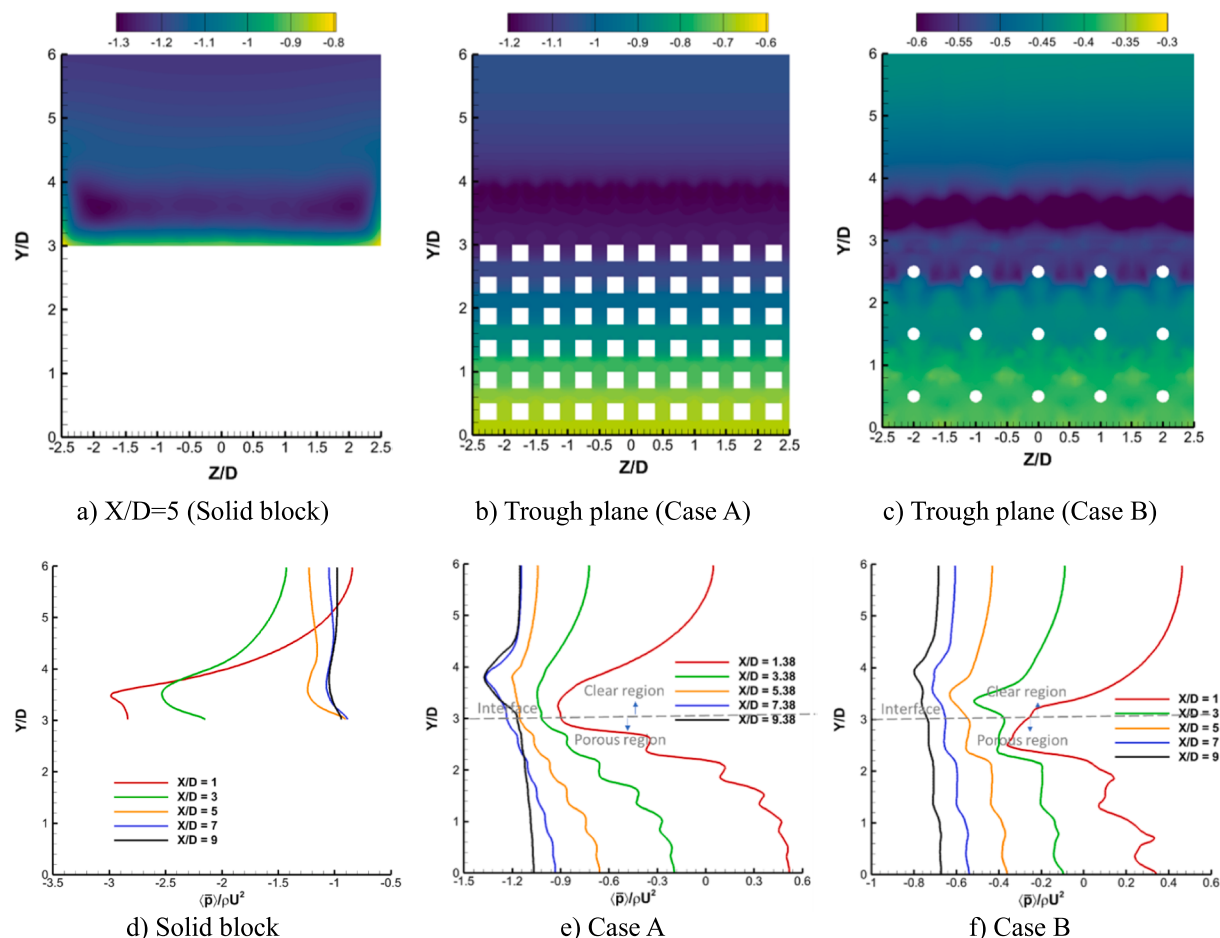


Fig. 15. Top: Side view on time-averaged pressure on trough plane; Bottom: Vertical distributions of pressure on trough plane at different streamwise locations along the porous block.

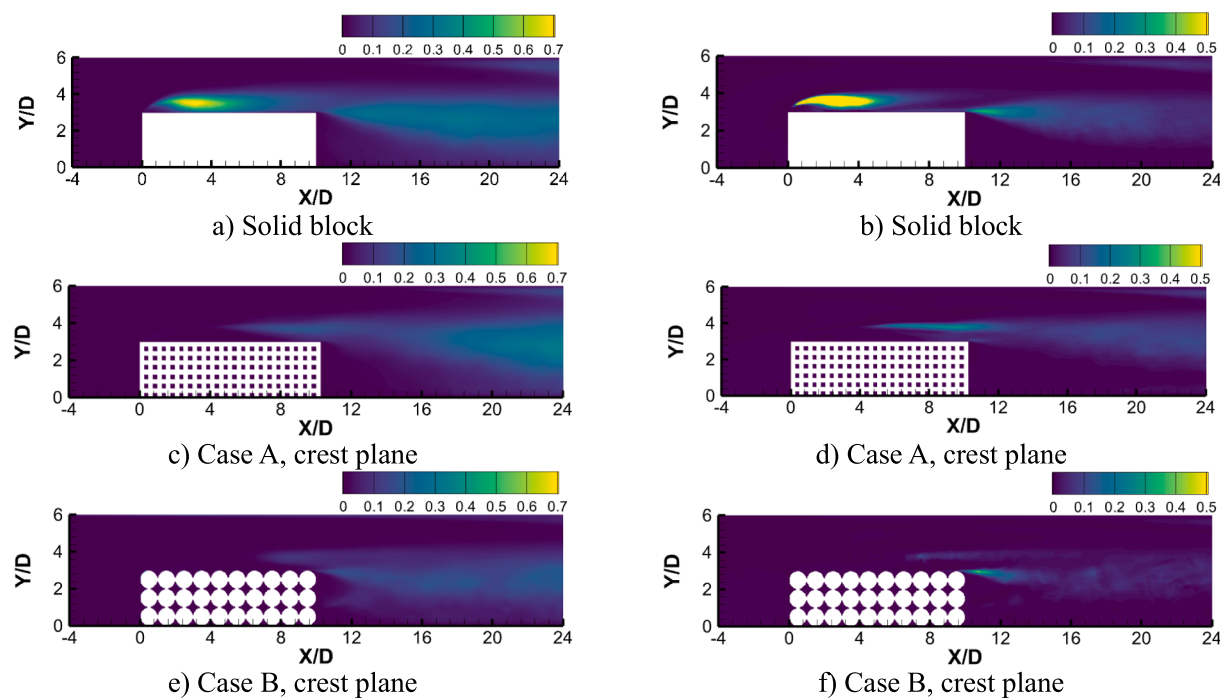


Fig. 16. Left: Front view contours of turbulent kinetic energy; Right: Contours of time-averaged turbulence production.

Table 3

Normalised magnitude of TKE at different locations above the interface.

X/D	TKE _{solid} (Solid block at Y/D = 3.53)	TKE/TKE _{solid} (Case A at Y/D = 4.02)	TKE/TKE _{solid} (Case B at Y/D = 3.72)
1.5	0.47	0.00	0.00
3	0.70	0.00	0.00
5	0.46	0.16	0.01
7	0.27	0.64	0.16
9	0.17	1.26	0.61

region. Comparison of pressure gradients at different streamwise locations along the porous block in Fig. 15 (e, f) shows that there is a very strong vertical pressure gradient at the beginning of the porous block, whereas at the end of the porous block it almost vanishes. This flow behaviour is consistent with the retardation of vertical distributions of streamwise velocity addressed in Fig. 7 and the higher tendency of leakage in the first half of the porous block argued in Table 2. Moreover, pressure distributions inside and outside of the porous blocks show two different behaviours, namely: a negative vertical pressure gradient inside the porous block and a positive pressure gradient outside of it. It is known that this kind of pressure profile can form a hairpin vortex which will be discussed in the following sub-section. For instance, Harun, et al. [53] showed that pressure gradient greatly influences the generation of large-scale flow structures associated with the outer layer in boundary layers. They found that large-scale motions are amplified in the adverse pressure gradient boundary layer, whereas they are attenuated in a favourable pressure gradient. This suggests that one of the effects of the adverse pressure gradient is to strengthen and/or increase the population of large-scale motions [53]. Based on the above discussion we can anticipate a propensity of flow laminarization for the porous block cases compared to the solid block case. This concept will be discussed in Section 3.4.

3.4. Turbulent statistics

Contours of turbulent kinetic energy, $TKE = 0.5(\bar{u}^2 + \bar{v}^2 + \bar{w}^2)$, and

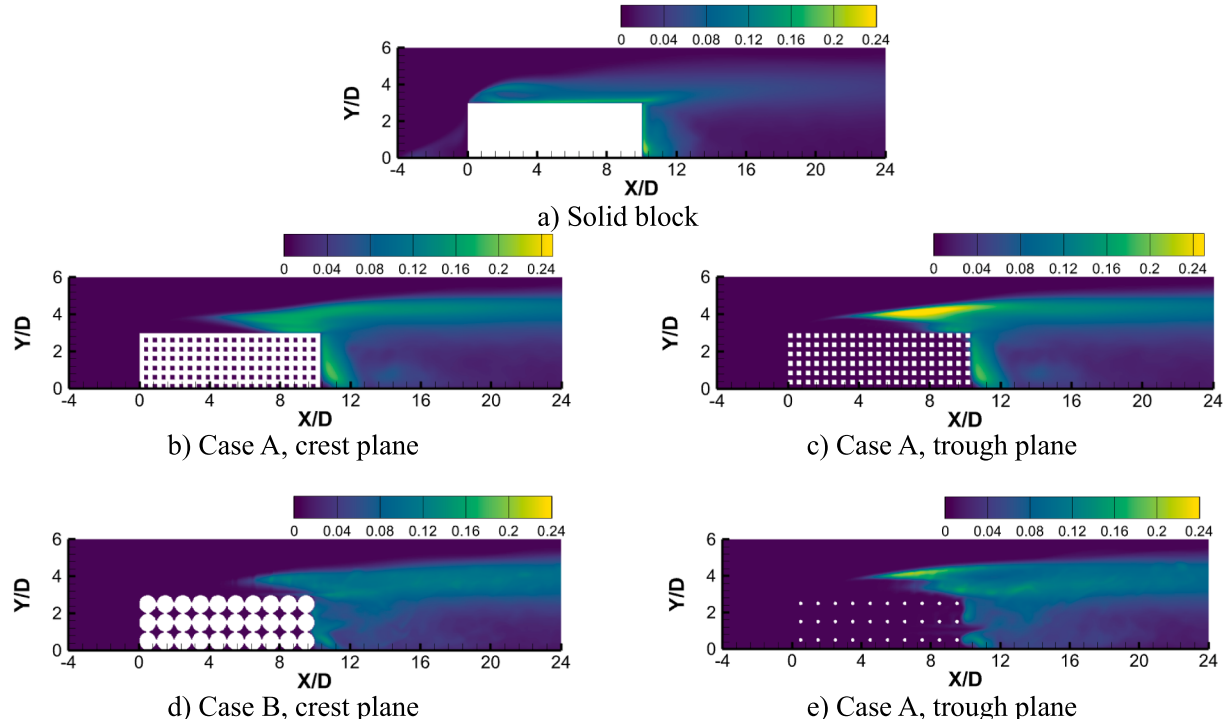


Fig. 17. Front view contours of non-dimensional temperature fluctuation; Left: Crest plane; Right: Trough plane.

turbulence production, ($P_k = -\bar{u}_i \bar{u}_j \partial \bar{u}_i / \partial X_j$), are shown in Fig. 16. Two distinct regions of TKE can be identified for the solid block case. The first region, with a significantly higher peak value, is located downstream of the leading edge of the solid block and matches the region where negative wall-normal velocities are observed (corresponding to the transport of high momentum fluid towards the wall). At this region, the flow is separated at the leading edge of the block and large turbulent energy is generated. The turbulence generated on the upstream edge of the block is then evolved quickly up to nearly $X/D = 4.19$, where the separated flow attaches again to the top surface (Fig. 16 (a, b)). However, for the porous blocks at this region, almost no turbulent kinetic energy is created on the leading edge of the structures. The normalized magnitude of TKE at different streamwise locations above the interface in Table 3 reveals that there is almost no turbulence production in the region of $0 < X/D < 3$ and $0 < X/D < 5$ for cases A and B respectively (flow laminarization).

Due to the flow leakage in the porous cases, the vertical distance of the TKE peaks from the interface is increased compared to the solid block case. For instance, for the solid block case, the peak value of TKE happens at $Y/D = 3.53$ (0.53D above the interface), while it detects at $Y/D = 4.02$ (1.02D above the interface) and $Y/D = 3.72$ (0.72D above the interface) for case A and B respectively. Since the flow leakage for case A is stronger than case B, the TKE peak is observed at a higher elevation for this case. The second region with a much lower or secondary peak is located downstream of the trailing edge above the leeward face of the solid block. This region coincides with the shear layer above the wake region which is associated with upward transport of low momentum fluid into the outer high-speed flow. Although the secondary peak in this region is observed for the porous blocks, its value is reduced significantly. For example, for the solid block case, the value of TKE at the secondary peak is 0.3, whereas it is diminished to 0.07 and 0.17 for cases A and B respectively. This observation suggests that the reduction in the TKE above the interface is linked to the deterioration of reverse flow (primary recirculation region) on the porous-fluid interface as discussed previously in Fig. 6.

Fig. 17 shows the distribution of temperature fluctuation (θ_{RSM}). This

figure confirms the previous findings in Fig. 16. It shows that over the porous interface the trend of temperature fluctuations matches with the turbulence production distribution. Due to the flow separation at the leading edge of the solid block and large turbulence production, the temperature fluctuates in this region. However, for the porous cases, almost no fluctuations are created on the leading edge of the blocks. The temperature fluctuations show that the transition to turbulence occurs at a location closer to the trailing edge of the porous block. For example, there are almost no temperature fluctuations in the region of $0 < X/D < 3$ and $0 < X/D < 5$ for cases A and B, respectively. While significant temperature fluctuation is observed at the leading edge ($X/D = 0$) of the solid block. These observations support the flow laminarization over the interface for the porous blocks.

4. Conclusions

Pore-scale LES investigation is conducted over a porous medium in a channel with two different porous blocks to explore heat and flow exchange between porous and non-porous regions as well as within the porous structure. For this purpose, two porous configurations with two different interface topographies are studied and the results are compared against those obtained for a solid block with the same size as the porous block. The main findings are summarized as follows:

- (1) The fluid entering the porous blocks is pushed upwards toward the porous-fluid interface and leaves the porous region halfway through to the non-porous region (flow leakage). The leakage clogs the horizontal channels inside the porous block which induces a significant reduction in streamwise momentum of the pore flow, especially at higher porous levels near the interface.
- (2) The boundary layer over the porous-fluid interface is continuously disrupted by the flow leakage across the interface. Flow visualization demonstrates the formation of organized counter-rotating vortex pairs (CRVPs) of fluid flow within and above the porous blocks due to the flow leakage. The CRVPs originate from the bottom of the porous block and move upwards altering the coherent structures of the flow above the interface.
- (3) Iso-surface of vortex strength above the porous interface shows a forest of vortices with a clear hairpin structure for all the cases. However, for the solid block, the hairpin structures are not as organized as the porous blocks. The distribution of streamlines indicates that the rotation of the legs and necks of the hairpin structures is consistent with the CRVPs above the porous interface.
- (4) Contours of instantaneous temperature show Kelvin-Helmholtz instabilities above the porous block interface. The shear layer above the interface is modified by Kelvin-Helmholtz instabilities and it is divided into three segments. The first segment is characterized by the flow separation at the leading edge of the porous block and the onset growth of the Kelvin-Helmholtz instabilities. At this part, the turbulence production is negligible and almost no TKE distribution is observed. In the second part of the shear layer, the Kelvin-Helmholtz instabilities are grown enough to lead to the formation of spanwise vortex structures. At this division, the higher values of velocity fluctuations occur. The third segment of the shear layer is characterized by cross interaction of wake and shear layer that leads to the deterioration of the coherent structures.
- (5) The distribution of turbulence production and turbulence kinetic show the flow laminarization above the interface for the porous block cases. Velocity and temperature fluctuations above the interface confirm that the shear layer above the top wall of the solid block has completed the transition to turbulence. However, for the porous blocks, no distinct fluctuations can be observed at the beginning of the porous block over the interface. This implies that for the porous blocks the transition to turbulence is

postponed to the end of the porous block and it is not achieved as fast as the solid block.

Declaration of Competing Interest

The authors declare that they have no known competing financial interests or personal relationships that could have appeared to influence the work reported in this paper.

Acknowledgement

This work was supported by the UK Engineering and Physical Sciences Research Council (EPSRC) [grant numbers EP/T012242/1 and EP/T012242/2]. Data supporting this publication can be obtained on request. The authors would like to acknowledge the assistance given by Research IT and the use of the Computational Shared Facility at The University of Manchester. The paper was presented and published in the proceedings of the 15th International Conference on Heat Transfer, Fluid Mechanics and Thermodynamics (HEFAT2021), Online, 26 – 28 July 2021.

References

- [1] O. Yasar, E. Ozbek, S. Ekici, E. Yalcin, A. Midilli, T.H. Karakoc, Assessment of fuel cell studies with particle image velocimetry applications: A key review, *Int. J. Hydrogen Energy* 46 (57) (2021) 29568–29582, <https://doi.org/10.1016/j.ijhydene.2021.05.027>.
- [2] K. Duan, L. Zhu, M. Li, L. Xiao, N. Bevilacqua, L. Eifert, I. Manke, H. Markötter, R. Zhang, R. Zeis, P.-C. Sui, Multiphase and porescale modeling on catalyst layer of high-temperature polymer electrolyte membrane fuel cell, *J. Electrochem. Soc.* 168 (5) (2021) 054521, <https://doi.org/10.1149/1945-7111/abff03>.
- [3] G.K. Marri, C. Balaji, Experimental and numerical investigations on the effect of porosity and PPI gradients of metal foams on the thermal performance of a composite phase change material heat sink, *Int. J. Heat Mass Transf.* 164 (2021) 120454, <https://doi.org/10.1016/j.ijheatmasstransfer.2020.120454>.
- [4] A.M. Ranjbar, Z. Pouransari, M. Siavashi, Improved design of heat sink including porous pin fins with different arrangements: A numerical turbulent flow and heat transfer study, *Appl. Therm. Eng.* 198 (2021) 117519, <https://doi.org/10.1016/j.applthermaleng.2021.117519>.
- [5] J. Duan, A novel heat sink for cooling concentrator photovoltaic system using PCM-porous system, *Appl. Therm. Eng.* 186 (2021) 116522, <https://doi.org/10.1016/j.applthermaleng.2020.116522>.
- [6] P.C. Huang, K. Vafai, Analysis of forced convection enhancement in a channel using porous blocks, *J. Thermophys. Heat Transfer* 8 (3) (1994) 563–573, <https://doi.org/10.2514/3.579>.
- [7] A. Amiri, K. Vafai, T. Kuzay, Effects of boundary conditions on non-Darcian heat transfer through porous media and experimental comparisons, *Numer. Heat Trans., Part A: Appl.* 27 (1995) 651–664, <https://doi.org/10.1080/10407789508913724>.
- [8] R. Attarzadeh, M. Rovira, C. Duwig, Design analysis of the “Schwartz D” based heat exchanger: A numerical study, *Int. J. Heat Mass Transf.* 177 (2021) 121415, <https://doi.org/10.1016/j.ijheatmasstransfer.2021.121415>.
- [9] Z.-Z. Li, Y.-D. Ding, Q. Liao, M. Cheng, X. Zhu, An approach based on the porous media model for numerical simulation of 3D finned-tubes heat exchanger, *Int. J. Heat Mass Transf.* 173 (2021) 121226, <https://doi.org/10.1016/j.ijheatmasstransfer.2021.121226>.
- [10] W.-J. Chang, W.-L. Chang, Mixed convection in a vertical parallel-plate channel partially filled with porous media of high permeability, *Int. J. Heat Mass Transf.* 39 (7) (1996) 1331–1342, [https://doi.org/10.1016/0017-9310\(95\)00234-0](https://doi.org/10.1016/0017-9310(95)00234-0).
- [11] P.C. Huang, K. Vafai, Flow and heat transfer control over an external surface using a porous block array arrangement, *Int. J. Heat Mass Transf.* 36 (16) (1993) 4019–4032, [https://doi.org/10.1016/0017-9310\(93\)90152-V](https://doi.org/10.1016/0017-9310(93)90152-V).
- [12] A. Leontiev, B. Kichatov, A. Korshunov, V. Gubernov, A. Kiverin, Effect of the flow rate of injected air on the temperature of porous wall in the supersonic flow, *Int. J. Heat Mass Transf.* 175 (2021) 121382, <https://doi.org/10.1016/j.ijheatmasstransfer.2021.121382>.
- [13] F. Selimefendigil, H.F. Öztop, Three dimensional unsteady heat and mass transport from six porous moist objects in a channel under laminar forced convection, *Appl. Therm. Eng.* 183 (2021) 116100, <https://doi.org/10.1016/j.applthermaleng.2020.116100>.
- [14] A. Zhao, X. Rui, B. Rong, G. Wang, Conjugate modeling of flow and simultaneous heat and mass transfer in convective drying of porous substances, *Appl. Therm. Eng.* 199 (2021) 117571, <https://doi.org/10.1016/j.applthermaleng.2021.117571>.
- [15] A. Shams, F. Roelofs, E.M.J. Komen, E. Baglietto, Large eddy simulation of a randomly stacked nuclear pebble bed, *Comput. Fluids* 96 (2014) 302–321, <https://doi.org/10.1016/j.compfluid.2014.03.025>.
- [16] E. Alonso, E. Rojas, Air solid packed-beds for high temperature thermal storage: Practical recommendations for predicting their thermal behaviour, *Appl. Therm.*

- Eng. 202 (2022) 117835, <https://doi.org/10.1016/j.aplthermaleng.2021.117835>.
- [17] C. Zhao, M. Opolot, M. Liu, F. Bruno, S. Mancin, R. Flewell-Smith, K. Hooman, Simulations of melting performance enhancement for a PCM embedded in metal periodic structures, *Int. J. Heat Mass Transf.* 168 (2021) 120853, <https://doi.org/10.1016/j.ijheatmasstransfer.2020.120853>.
- [18] Y. Wang, Y.-i. Yu, Z. Jing, C. Wang, G. Zhou, W. Zhao, Thermal performance of lithium-ion batteries applying forced air cooling with an improved aluminium foam heat sink design, *J. Heat Mass Transfer* 167 (2021) 120827, <https://doi.org/10.1016/j.ijheatmasstransfer.2020.120827>.
- [19] K. Anirudh, S. Dhinakaran, Performance improvement of a flat-plate solar collector by inserting intermittent porous blocks, *Renew. Energy* 145 (2020) 428–441, <https://doi.org/10.1016/j.renene.2019.06.015>.
- [20] P.-C. Huang, C.-C. Chen, H.-Y. Hwang, Thermal enhancement in a flat-plate solar water collector by flow pulsation and metal-foam blocks, *Int. J. Heat Mass Transf.* 61 (2013) 696–720, <https://doi.org/10.1016/j.ijheatmasstransfer.2013.02.037>.
- [21] C.-C. Chen, P.-C. Huang, Numerical study of heat transfer enhancement for a novel flat-plate solar water collector using metal-foam blocks, *Int. J. Heat Mass Transf.* 55 (23–24) (2012) 6734–6756, <https://doi.org/10.1016/j.ijheatmasstransfer.2012.06.082>.
- [22] W.-S. Fu, H.-C. Huang, W.-Y. Liou, Thermal enhancement in laminar channel flow with a porous block, *Int. J. Heat Mass Transf.* 39 (10) (1996) 2165–2175, [https://doi.org/10.1016/0017-9310\(95\)00208-1](https://doi.org/10.1016/0017-9310(95)00208-1).
- [23] S.C. Tzeng, Convective heat transfer in a rectangular channel filled with sintered bronze beads and periodically spaced heated blocks, *J. Heat Transfer* 128 (2006) 453–464, <https://doi.org/10.1115/1.2175151>.
- [24] X.u. Chu, W. Wang, G. Yang, A. Terzis, R. Helmig, B. Weigand, Transport of turbulence across permeable interface in a turbulent channel flow: Interface-resolved direct numerical simulation, *Transp. Porous Media* 136 (1) (2021) 165–189, <https://doi.org/10.1007/s11242-020-01506-w>.
- [25] Y. Kuwata, K. Suga, Transport mechanism of interface turbulence over porous and rough walls, *Flow Turbulence Combust.* 97 (4) (2016) 1071–1093, <https://doi.org/10.1007/s10494-016-9759-9>.
- [26] A. Leonardi, D. Pokrajac, F. Roman, F. Zanello, V. Armenio, Surface and subsurface contributions to the build-up of forces on bed particles, *J. Fluid Mech.* 851 (2018) 558–572, <https://doi.org/10.1017/jfm.2018.522>.
- [27] F. Shikh Anuar, K. Hooman, M.R. Malayeri, I. Ashtiani Abdi, Experimental study of particulate fouling in partially filled channel with open-cell metal foam, *Exp. Therm Fluid Sci.* 110 (2020) 109941, <https://doi.org/10.1016/j.expthermflusci.2019.109941>.
- [28] A.A. Servati V., K. Javaherdeh, H.R. Ashorynejad, Magnetic field effects on force convection flow of a nanofluid in a channel partially filled with porous media using Lattice Boltzmann Method, *Adv. Powder Technol.* 25 (2) (2014) 666–675, <https://doi.org/10.1016/j.apt.2013.10.012>.
- [29] T. Kim, G. Blois, J.L. Best, K.T. Christensen, Experimental study of turbulent flow over and within cubically packed walls of spheres: Effects of topography, permeability and wall thickness, *Int. J. Heat Fluid Flow* 73 (2018) 16–29, <https://doi.org/10.1016/j.ijheatfluidflow.2018.06.004>.
- [30] Y. Kuwata, K. Suga, Extensive investigation of the influence of wall permeability on turbulence, *Int. J. Heat Fluid Flow* 80 (2019) 108465, <https://doi.org/10.1016/j.ijheatfluidflow.2019.108465>.
- [31] D. Pokrajac, C. Manes, I. McEwan, Peculiar mean velocity profiles within a porous bed of an open channel, *Phys. Fluids* 19 (9) (2007) 098109, <https://doi.org/10.1063/1.2780193>.
- [32] G.S. Beavers, D.D. Joseph, Boundary conditions at a naturally permeable wall, *J. Fluid Mech.* 30 (1) (1967) 197–207, <https://doi.org/10.1017/S0022112067001375>.
- [33] B. Alazmi, K. Vafai, Analysis of fluid flow and heat transfer interfacial conditions between a porous medium and a fluid layer, *Int. J. Heat Mass Transf.* 44 (9) (2001) 1735–1749, [https://doi.org/10.1016/S0017-9310\(00\)00217-9](https://doi.org/10.1016/S0017-9310(00)00217-9).
- [34] Y. Mahmoudi, N. Karimi, K. Mazaheri, Analytical investigation of heat transfer enhancement in a channel partially filled with a porous material under local thermal non-equilibrium condition: Effects of different thermal boundary conditions at the porous-fluid interface, *Int. J. Heat Mass Transf.* 70 (2014) 875–891, <https://doi.org/10.1016/j.ijheatmasstransfer.2013.11.048>.
- [35] P. Forooghi, M. Akbar, M. Saffar-Aval, Steady and unsteady heat transfer in a channel partially filled with porous media under thermal non-Equilibrium condition, *Transp. Porous Media* 86 (1) (2011) 177–198, <https://doi.org/10.1007/s11242-010-9615-7>.
- [36] R.J. Adrian, C.D. Meinhart, C.D. Tomkins, Vortex organization in the outer region of the turbulent boundary layer, *J. Fluid Mech.* 422 (2000) 1–54, <https://doi.org/10.1017/S0022112000001580>.
- [37] B. Alazmi, K. Vafai, Constant wall heat flux boundary conditions in porous media under local thermal non-equilibrium conditions, *Int. J. Heat Mass Transf.* 45 (2002) 3071–3087, [https://doi.org/10.1016/S0017-9310\(02\)00044-3](https://doi.org/10.1016/S0017-9310(02)00044-3).
- [38] M. Torabi, N. Karimi, K. Zhang, Heat transfer and second law analyses of forced convection in a channel partially filled by porous media and featuring internal heat sources, *Energy* 93 (2015) 106–127, <https://doi.org/10.1016/j.energy.2015.09.010>.
- [39] F. Shikh Anuar, I. Ashtiani Abdi, K. Hooman, Flow visualization study of partially filled channel with aluminium foam block, *Int. J. Heat Mass Transf.* 127 (2018) 1197–1211, <https://doi.org/10.1016/j.ijheatmasstransfer.2018.07.047>.
- [40] B. Alazmi, K. Vafai, Analysis of variants within the porous media transport models, *J. Heat Transfer* 122 (2000) 303–326, <https://doi.org/10.1115/1.521468>.
- [41] W.P. Breugem, B.J. Boersma, R.E. Uittenbogaard, The influence of wall permeability on turbulent channel flow, *J. Fluid Mech.* 562 (2006) 35, <https://doi.org/10.1017/s0022112006000887>.
- [42] J.J. Voermans, M. Ghisalberti, G.N. Ivey, The variation of flow and turbulence across the sediment–water interface, *J. Fluid Mech.* 824 (2017) 413–437, <https://doi.org/10.1017/jfm.2017.345>.
- [43] S.B. Pope, *Turbulent Flows*, Cambridge University Press, Cambridge, 2000.
- [44] W.-W. Kim, S. Menon, W.-W. Kim, S. Menon, Application of the localized dynamic subgrid-scale model to turbulent wall-bounded flows, in: 35th aerospace sciences meeting and exhibit, 1997, pp. 210.
- [45] W.M. Kays, *Turbulent Prandtl Number—Where Are We?* *J. Heat Transfer* 116 (1994) 284–295, <https://doi.org/10.1115/1.2911398>.
- [46] H. Jasak, A. Jemcov, Z. Tukovic, OpenFOAM: A C++ library for complex physics simulations, in: International workshop on coupled methods in numerical dynamics, Vol. 1000, IUC Dubrovnik Croatia, 2007, pp. 1–20.
- [47] H.K. Versteeg, W. Malalasekera, *An Introduction to Computational Fluid Dynamics: the Finite Volume Method*, 2nd ed., Pearson Education Limited, Harlow, England, 2007.
- [48] F. Bazdidi-Tehrani, A. Ghafouri, M. Jadidi, Grid resolution assessment in large eddy simulation of dispersion around an isolated cubic building, *J. Wind Eng. Ind. Aerodyn.* 121 (2013) 1–15, <https://doi.org/10.1016/j.jweia.2013.07.003>.
- [49] L. Davidson, *How to estimate the resolution of an LES of recirculating flow*, in: *Quality and Reliability of Large-Eddy Simulations II*, Springer, Netherlands, 2011, pp. 269–286.
- [50] J.M. Leu, H.C. Chan, M.S. Chu, Comparison of turbulent flow over solid and porous structures mounted on the bottom of a rectangular channel, *Flow Meas. Instrum.* 19 (6) (2008) 331–337, <https://doi.org/10.1016/j.flowmeastinst.2008.05.001>.
- [51] R. Poletto, T. Craft, A. Revell, A new divergence free synthetic eddy method for the reproduction of inlet flow conditions for LES, *Flow Turbulence Combust.* 91 (3) (2013) 519–539, <https://doi.org/10.1007/s10494-013-9488-2>.
- [52] W.P. Breugem, B.J. Boersma, R.E. Uittenbogaard, The laminar boundary layer over a permeable wall, *Transp. Porous Media* 59 (3) (2005) 267–300, <https://doi.org/10.1007/s11242-004-2557-1>.
- [53] Z. Harun, J.P. Monty, R. Mathis, I. Marusic, Pressure gradient effects on the large-scale structure of turbulent boundary layers, *J. Fluid Mech.* 715 (2013) 477–498, <https://doi.org/10.1017/jfm.2012.531>.